Intra-night flickering of MWC 560: Parameters and quasi-period modes. Comparison with RS Oph and T CrB

Ts. B. Georgiev, S. Boeva, K. A. Stoyanov,
G. Latev, B. Spassov, A. Kurtenkov
Institute of Astronomy and National Astronomical Observatory,
Bulgarian Academy of Sciences, 72 Tsarigradsko Chaussee Blvd., 1784 Sofia, Bulgaria
tsgeorg@astro.bas.bg
(Submitted on 07.10.2021. Accepted on 15.01.2022)

Abstract. We analysed 15 B-band and 15 V-band light curves (LCs) of the flickering-active symbiotic star MWC 560, observed over 2009–2018 by 4 Bulgarian telescopes. The LCs are linearized, flattened and analysed by a method, developed earlier for the cases of RS Oph [G20] and T CrB [G21], represented here with some justifications.

We find that the flickering statistics of RS Oph, T CrB and MWC 560 are similar, although MWC 560 shows some deficit of short sharp peaks and its logarithms of the flux standard deviations and the flux range deviations pose correlation coefficients of 0.99. In comparison with the other stars the flickering of MWC 560 also shows an intermediate mean skewness, with some excess of positive deviations, but a lower mean kurtosis, i.e. a deficit of large deviations. The kurtosis obeys a quadratic correlation with the skewness. Among the mentioned 3 stars the flickering of MWC 560 poses the highest structure gradient, i.e. the most significant non-sharp shots and the lowest Hurst gradient, i.e. the highest chaos.

We reveal quasi-periods (QPs) in the flickering by locating the minima of the structure functions and the relevant maxima of the autocorrelation functions. We reveal 51 QPs of MWC 560 with 8 modes, accurately obeying a power function with a base of $1.34 \approx 4/3$. For RS Oph and T CrB the bases are $\approx 3/2$ and ≈ 2. The regularities (near-commensurabilities) of the modes of these 3 stars are very different, for yet unknown reasons. The most frequent QPs of the stars in question are 21 min, 20 min and 23 min, respectively. Our empirical asymmetry function of the flickering gives an estimator of the shortest QP, depending on the observing conditions. For the mentioned stars they are 2.6 min, 1.2 min and 3.5 min, respectively. These QPs fall approximately on the prolongations of the regularity models of the QP modes towards the short times.

Key words: stars: binaries: symbiotic – novae, cataclysmic variables – stars: individual: MWC 560.

Introduction

MWC 560 (V694 Mon) is a symbiotic star consisting of a M5.5 giant (Schmid et al. 2001) and an accreting white dwarf with a mass of 0.85–1.0 $M_{\odot}$ (Zamanov, Gomboc & Latev 2011). The most remarkable feature of MWC 560 is the powerful collimated outflow extended up to 6000–7000 km/s (Tomov et al. 1990). The outflow could be a highly-collimated baryon-loaded jet (Schmid et al. 2001) or a wind from the polar regions (Lucy, Knigge & Sokoloski 2018).

MWC 560 is considered to be a low-mass non-relativistic analogue of quasars not only because of its jets, but also for the resemblance of its emission lines to that of the low-redshift quasars (Zamanov & Marziani 2002) and its absorption lines to that of the broad absorption line quasars (Lucy, Knigge & Sokoloski 2018). It is accepted that the orbital period of the system is $P_{orb} = 1931 \pm 162$ d (Gromadzki et al. 2007), although Munari et al. (2016a) proposed a considerably shorter orbital period, $P_{orb} \approx 330.8$ d. The orbital eccentricity is 0.68–0.82 (Zamanov et al. 2010). The distance to the system is about 2.5 kpc (Lucy et al. 2020).

During the recent decades two optical outbursts of MWC 560 were detected. The first one took place in 1990 (Tomov et al. 1990). The second outburst, even brighter than the previous, began in 2016 (Munari et al. 2016b). The 2016 optical outburst was followed by enhanced X-ray (Lucy et al. 2016a) and radio emissions (Lucy, Weston & Sokoloski 2016b).

MWC 560 is one of the flickering-active symbiotic stars. The optical flickering from the system is detected by Bond et al. (1984). Tomov et al. (1996, Fig. 6) report an amplitude of the flickering in the range 0.1–0.7 mag and quasi-periods (QPs) from 11 to 160 min. The flickering was a persistent feature till 2018, when the variability on a time scale of minutes became undetectable (Goranskij et al. 2018).

Zamanov et al. (2021), hereafter Z21, carried out 17 quasi-simultaneous observations of MWC 560 in 2009–2019 with 4 Bulgarian telescopes with a photometric errors of 0.004 mag in B- and 0.005 mag in V- band. They found that the hot component becomes redder as it gets brighter, while the flickering source has colour (B-V) 0.14–0.40, temperature 6300–11000 K (as in the bright spots of cataclysmic variables) and radius 1.2–18 $R_{\odot}$. They also found a correlation between the B-magnitude and the radius of the flickering source. In 2019 the flickering disappeared and the hot component became bluer and brighter.

The goals of the present paper are (i) to briefly represent the method with some justifications, (ii) to analyse statistical and fractal parameters of the flickering, as well as (iii) to reveal QPs and their modes.

The fractal methods applied here are preferable because (i) they are conceptually simple, (ii) they are weakly sensitive to non-equality of the data sampling and (iii) in contrast with the Fourier method they are well applicable at low signal-to-noise ratio of the QPs. Such an approach has been applied by Georgiev et al. (2020), hereafter G20, and Georgiev et al. (2021), hereafter G21, for analysis of the flickering of the symbiotic stars RS Oph and T CrB, respectively (see Fig. 7).

The contents are as follows:
1. Light curves and parameters
2. Fractal functions and parameters
3. Quasi-periods and modes
4. Other results

This paper also contains Conclusions; Bibliography and on-line Appendix.

The Appendix is available only in electronic form on the site of the Bulgarian Astronomical Journal, Vol.37. It contains 2 tables with data of 30 observing runs and found quasi-periods, as well as 28 panels that illustrate the processing details. The runs #03b and #03v are shown here in Fig. 1 and Fig. 2.

The used abbreviations and subscripts follow:
AF – asymmetry (ratio) function, Sect. 2, Figs. e;
AV – average value;
BT – breakdown time point of the AF, Sect. 2, Figs. e;
CC – correlation coefficients;
CF – (auto)correlation function, Sect. 2, Figs. f;
DF – (standard) deviation function, Sect. 2, Figs. d;
FD – fractal dimension, Sect. 2;
FLC – residual light curve, Sect. 1, Figs. b;

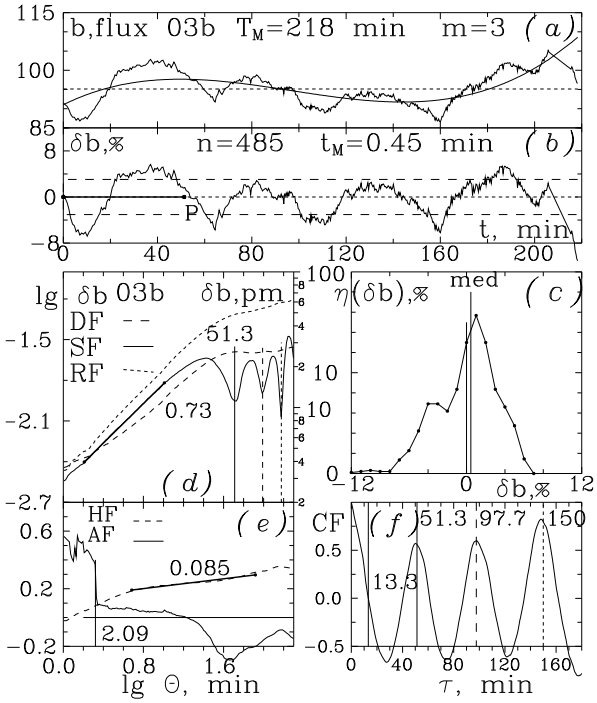

Fig. 1. Run #03b in B-band. **(a)**: LLC with monitoring time $T_{\rm M}$, fit of m-th degree and average level; **(b)**: FLC with n data, mean time resolution $t_{\rm M} = T_{\rm M}/n$ and QP size (horizontal) P min, found in (d) and (f); **(c)**: Histogram of the deviations of the FLC (b) with positions of the AV and median; **(d)**: DF, RF (Eq. 1) and SF (Eq. 2) of the FLC versus the fractal window Θ, in log-log scales, with $SG = 0.73$ (solid segment). The positions of the minima of the SF, marked by verticals, are QPs. The leftmost QP, with $P = 51.3$ min, is accepted as the main QP of the run. Other QPs, $2P, 3P$, are ignored as "harmonics". Note that the right ordinate is graduated per mils (pm); **(e)**: HF (Eq. 3) and AF (Eq. 4) in log-log scales with $HG = 0.085$ (solid segment) and $BT = 2.09$ min (vertical marker); **(f)** CF (Eq. 5) with correlation time, 13.3 min, marked by the leftmost vertical. The positions of the maxima of the CF, marked by verticals, are QPs, in minutes, corresponding to the minima of the SF in (d). The horizontal is the zero level. (See the text.)

HF – Hurst function, Sect. 2, Figs. e;
HG – Hurst gradient, Sect. 2, Figs. e;
LC – light curve, Sect. 1;
LLC – linearized light curve, Sect. 1, Figs. a;
QP – quasi-period in the FLC, Sect. 2, Figs. d,f;
RD – range deviation, Sect. 1;
RF – range function, Sect. 2, Figs 1, 2;
SD – standard deviation, Sect. 1;
SF – structure function, Sect. 2, Figs. d;
SG – structure gradient, Sect. 2, Figs. d;

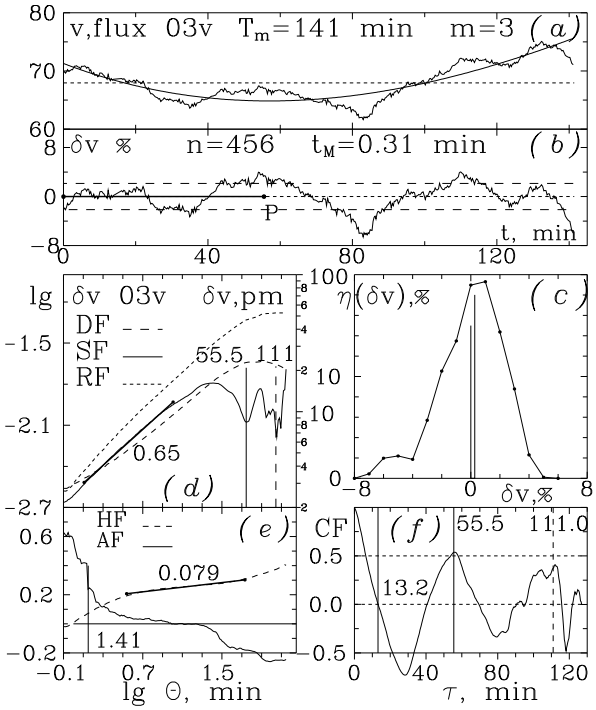

Fig. 2. Run #03v in V-band. **(a)**: LLC; **(b)**: FLC; **(c)**: Histogram of the FLC deviations (b); **(d)**: DF, RF and SF with SG and marked QPs; **(e)**: HF with HG and AF with BT; **(f)**: CF with marked QPs. See Fig. 1.

Note that the sub-figures in Fig. 1, Fig. 2, as well as in all panels in the Appendix, for example "b", will be cited hereafter shortly as "Figs. b".

1. Light curves and parameters

Two kinds of LCs are used here. The first one of them, $b(t)$ or $v(t)$, is a linearized LC (LLC), transformed from magnitudes to fluxes in

10^{-14} erg cm^{-2} s^{-1} $\AA^{-1}$ (Z21). The second one, $\delta b(t)$ or $\delta v(t)$, is a flattened (residual) LC (FLC).

The LLC (Figs. a) is used for deriving the statistics of the flickering and for the fitting and removal of a large scale trend. The LLC is a time series and it may be generally characterized by the basic statistics: average value (AV), a_B, a_V, standard deviation (SD), s_B, s_V and range deviation (RD), r_B, r_V. In this paper the RD is the half of the peak-to-peak amplitude in order to be compatible with the SD. Thus our respective range function (Eq. 1) is not very high and it may be easily included in Figs. d, if needed, as in Figs. 1d, 2d.

Figure 3 juxtaposes the absolute flux statistics of the LLCs.

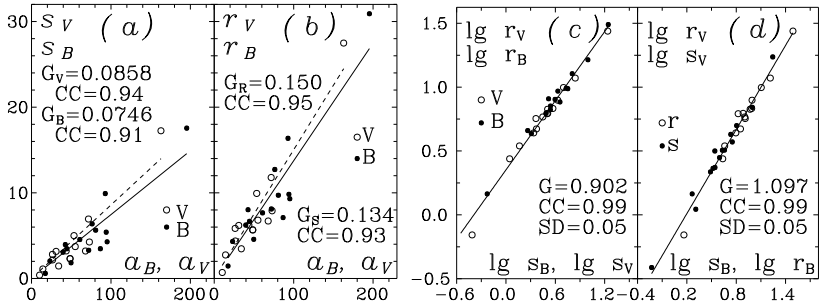

Fig. 3. (a,b): Separate and mutual correlations of the SDs (s) and RDs (r) with the AVs (a) of the LLCs in B-band (dots, solid lines) and in V-band (circles, dashed liness). The linear fits are built to pass through the coordinate zero. Hereafter G is the gradient (slope coefficient) of the fit and CC is the correlation coefficient; **(c,d):** Sparate and mutual correlations between the logarithms of the SDs and the RDs of the LLCs in B- and V- band (see the text).

Figures 3a, 3b show the expected flux correlations between the SDs and the RDs with the AVs of the LLCs. The average gradients in B- and V- band, s/a and r/a, are 0.08 and 0.14. Zamanov et al. (2016), hereafter Z16, derived these for 9 symbiotic and cataclysmic stars (including RS Oph, T CrB and MWC 560) and found that their mean values are 0.08 and 0.35, respectively. Accounting for the factor 1/2 towards our definition of RD, the value of r/a becomes 0.175. The flickering of MWC 560 poses smaller deviations.

Figures 3c, 3d show high mutual correlations between the logarithmic flux values of the SD and the RD, lg$s$ and lg$r$, in B- and V- band. In both cases the correlation coefficient (CC) is 0.99. Figure 3c juxtaposes together lgr_B versus lgs_B and lgr_V versus lgs_V, with a gradient $G = 0.902$, while the mean G for the 9 stars in Z16 is 1.002 (Z16, Eqs. 3, 4). Figure 3d juxtaposes together lgs_V versus lgs_B and lgr_V versus lgr_B with a gradient $G = 1.097$. Since the larger flickering peaks are redder (Z21), the slightly positive gradient is expected. See also Figs. 9b, 9c. So, with respect to the 9 analogous stars (Z16) the SDs of MWC 560 are similar, but the relevant RDs are lower by 10–20%.

Other statistics of the distributions of the LLC deviations are the skewness (asymmetry of the wings), A, and the kurtosis (contribution of the tails in respect to the contribution of the central part), E. In comparison with the normal distribution a positive A-value corresponds to a heavier positive wing (and vice versa), while a positive E-value corresponds to a distribution with heavy tails (and vice versa). In this paper we explore long time series and we apply just the definitions for A and E, without coefficients for short series (see G21). We also use a modified kurtosis $E' = \lg(E/3)$. This E' falls into the range $-0.4 - 0.6$ and it obeys a quadratic dependence on A within its range $-1.5 - 1.5$ (see Fig. 4c here and Fig. 6a in Georgiev 2022).

However, the LLCs (Figs. a) also contain fragments of multi-hour variabilities. They are obstructive for the QP detection. For this reason we are forced to fit and remove the large scale trend of the LLC by a polynomial fit. By removing the fit from the LLC we derive a residual (flattened) LC (FLC).

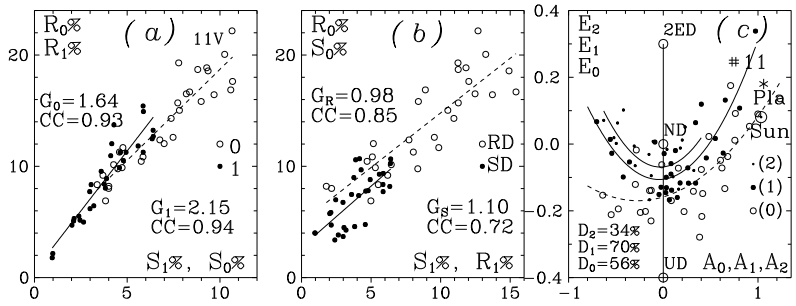

Fig. 4. (a,b): Correlations between the relative SDs and RDs in B- and V-band, together. **(a):** Mutual correlations R_0 vs. S_0 (from LLCs, circles) and R_1 vs. S_1 (from FLCs, dots); **(b):** Separate correlations R_0 vs. R_1 (circles) and S_0 vs. S_1 (dots) **(c)**: Quadratic correlation between the skewness A and the kurtosis E' for 30 LLCs (0), for 30 basic FLCs (1) and for 20 additional FLCs (derived for shorter QPs). The values of D_0, D_1, D_2 are the respective determination coefficients. The vertical segment contains the points of known symmetric distributions: uniform (UD, $E = 6/5$, $E' = -0.4$), normal (ND, $E = 3$, $E' = 0$) and double exponential (2ED, $E = 6$, $E' = 0.3$). The position of the time series of Wolf numbers of the Sun and the visits of the Smolyan Planetarium (G20) are marked on the right edge.

The FLC (Figs. b) is used for deriving statistical and fractal parameters and for revealing QPs. The FLC is a relative LC, expressed in percent of the polynomial level. It has an AV of zero. In this paper the FLC is also illustrated by a (histogram) distribution of its deviations (Figs. c). Figure 4 juxtaposes the flux statistics of the FLCs in B- and V-band together.

Figures 4a, 4b show the mutual and separate correlations between the relative SDs, $S = s/a$, and RDs, $R = r/a$. The subscripts "0" or "1" specify data from LLC or FLC, respectively. The effect of the trend removal is small in 4b, but it causes a significant decrease of the score and the gradient in 4a. The gradient R1 versus S1 is 2.15 while for RS Oph it is 2.43 (G20) and for T CrB it is 2.83 (G21). It is the lowest for MWC 560 due to its low RDs.

The histograms distributions of the skewness and the kurtosis for MWC 560, which are not shown here, are similar to those for RS Oph (G20, Figs. 3a, 3b) and T CrB (G21, Figs. 5a, 5b). However, the mutual distribution here is different and interesting.

Figure 4c juxtaposes the skewness A and the modified kurtosis E' of 30 LLCs (circles), 30 FLCs (dots; the trend is removed by polynomials of 1–4th degree) and 30 additional FLCs (small dots; the trend is removed by polynomials of 5–9th degree for revealing of shorter QPs). These distributions significantly depend on the goodness of the trend removals, but they all show quadratic shapes, as in the general case (Georgiev 2022, Fig. 6a). The skewness A is often positive, i.e. the positive twinkles at short time scale are more frequent. The mean kurtosis E' is slightly below zero, i.e. the large short deviations are rare. In comparison with RS Oph (with a larger deficit of short deviations) and T CrB (with some excess of large positive deviations) MWC 560 shows an intermediate mean skewness and a lower mean kurtosis (see Table 1).

Table 1. Comparison between the parameters of 3 symbiotic stars. $R_1/S_1, CC$ – gradient and CC of the relative values RD vs. SD; AV and SD of the skewness A for the FLCs; AV and SD of the kurtosis E' for the FLCs; AV and SD of the structure gradient SG for the FLCs; AV and SD of the Hurst gradient HG for the FLCs.

Star	RS Oph (B,V)		T CrB	(U)	MWC 560 (B,V)	
$R_1/S_1, CC$	2.43	0.90	2.63	0.90	2.15	0.93
$A_{\rm AV}, A_{\rm SD}$	0.08	±0.26	0.24	±0.16	0.13	±0.39
$E'_{\rm AV}, E'_{\rm SD}$	0.17	±0.21	0.02	±0.19	-0.04	±0.11
$SG_{\rm AV}, SG_{\rm SD}$	0.48	±0.16	0.34	±0.12	0.61	±0.10
$HG_{\rm AV}, HG_{\rm SD}$	0.22	±0.06	0.18	±0.05	0.16	±0.07

2. Fractal functions and parameters

Some useful fractal functions over the FLC, in log-log scales, may reveal specific properties of the flickering (G20, G21). Following the recommendations of Mandelbrot (1982), Russ (1994) and Falkoner (1997), we use the simplest such functions. They are shown in Figs. d, e, f.

In this paper the discrete FLC is assumed as $\delta u(t_n), n = 1, 2, ..., N$, where u replaces b (for B-band) or v (for V-band). The fractal characterizing of the FLC is based on a system of scanning time windows with sizes $\Theta_j, j = 1, 2, ..., J$, e.g. $J = 99$. These window sizes are designed to be distributed uniformly by lg Θ. Each j-th window scans the FLC taking $k = 1, 2, ..., K$ different positions. The k-th position of the j-th window gives fractal indicators, e.g. $\delta u_{\rm SD}(\Theta_j)_k$ and $\delta u_{\rm RD}(\Theta_j)_k$. The value of each indicator, averaged over all K positions of the j-th window, gives relevant fractal parameters, e.g. $< \delta u_{\rm SD}(\Theta) >_j$, $< \delta u_{\rm RD}(\Theta) >_j$. Hereafter the angle brackets mean averaging of the indicator for all K positions of the window Θ_j. The dependence of the fractal parameter on the window size, in log-log scale, is considered a fractal function.

The (standard) deviation function (DF) and the range (deviation) function (RF) describe the increase of the respective parameter, characterizing the "roughness" or "jaggedness" of the FLC with the increase of the window size Θ. The DF and RF are defined as follows:

$$DF_j(\Theta) =< \delta u_{\rm SD}(\Theta) >_j, \qquad RF_j(\Theta) =< \delta u_{\rm RD}(\Theta) >_j . \tag{1}$$

Figures d represent DFs by dashed curves. The RFs are considered to be less interesting. They are shown here only in Figs. 1d and 2d, as well as in all cases in G20.

When the window size Θ is small and increases, it incorporates larger FLC structures. The DF and the RF increase too. When the largest structures are exhausted, the DF tends to a plateau, corresponding to the SD of the whole FLC. The RF has higher values and continues to increase, but with a decreased rate (Figs. 1d, 2d). An important product of the RF is the rescaled RF or Hurst function (Eq. 3; Figs. e).

The structure function (SF) of the FLC is based on a structure indicator – the absolute difference between the FLC values at the bounds of the window Θ. The value of the FLC at the bound of the window is derived using a linear interpolation between the nearest two FLC values (G20, Fig. 4a). The average

value of this indicator over its K positions gives the structure parameter SF_j. The structure gradient (SG) characterizes the slope of the initial quasi-linear part of the SF. The SF and the SG are defined, as follows:

$$SF_j(\Theta) =< \delta u(t+\Theta) - \delta u(t) >_j, \qquad SG = \Delta \lg (SF) \ / \ \Delta \lg \Theta. \qquad (2)$$

Figures d represent the SFs by solid curves and the SGs by solid segments.

As the window Θ increases, it incorporates larger structures. The SF increases too, trending to a plateau. However, in contrast with the DF, when the Θ includes one or more QP structures entirely, the quantity of the new larger variations decreases. Then the SF shows one or more local minima (G20, Fig. 4a). The time position P of every minimum corresponds to the characteristic size of some structure, i.e. to some QP (Figs. d). The application of the SF as a QP detector is equivalent to the "phase dispersion minimization technique" of Lafler & Kinman (1965) (see Ganchev et al. 2017, Fig. 5, G20 and G21).

The SG of the SF contains information about the feedback of the flickering (di Clemente et al. 1996; Kawaguchi et al. 1998). A value of $SG < 0.5$ corresponds to prevalence of global flux instabilities of the flickering source and lower variability of the LC. A value of $SG > 0.5$ indicates a variability, driven mainly by separate shots, causing high variability of the LC.

The dwarf nova KR Aur has a $SG < 0.35$, which gives a hint that the so called self-organized criticality within an accretion disk may drive the variability of the noise continuum (Bachev et al, 2011). The SGs of RS Oph, T CrB and MWC 560 are 0.48, 0.34 and 0.61, respectively (Table 1). Therefore, the flickering of MWC 560 contains a significant contribution of shots (Fig. 1d). For comparison, the SG for the Wolf number of the Sun is similar, 0.56, the shots are the Sun cycles.

The rescaled RF, known as Hurst function (HF), describes the increase of the ratio $RF_j \ / \ DF_j$ when the window Θ increases. The Hurst gradient (HG) is the slope coefficient of the intermediate quasi-linear part of the HF. The HF and the HG are defined as follows:

$$HF_j(\Theta) =< \delta u_{RD}(\Theta)/\delta u_{SD}(\Theta) >_j, \quad HG = \Delta \lg (HF) \ / \ \Delta \lg \Theta. \qquad (3)$$

Figures e represent the HFs in log-log scale by dashed curves and the HGs by solid segments.

Hurst (1951) analyzed the fluctuations in the cumulative discharge of the Nile River and found that it is scaled self-similarly. He defined the rescaled RF by the full range deviation, i.e. by the "peak-to-peak amplitude". In G20, G21 and here we define and apply the RF by "the half of the peak-to-peak amplitude" (Eq. 1). By this reason our HG is lower towards the HG of Hurst by $lg2 = 0.3$. Hurst (1951) derived $HG = 0.77$ for the Nile River and our relevant value is $HG = 0.47$.

The HG characterizes the autocorrelation in the FLC (Mandelbrot & Wallis 1968). For our definition a value of $HG < 0.2$ indicates a time series with a short-term positive autocorrelation, i.e. with higher chaos. Our value of $HG > 0.2$ indicates a time series with a long-term positive autocorrelation, i.e with lower chaos.

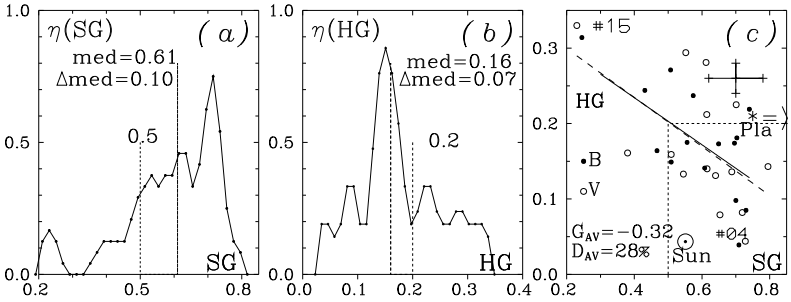

Fig. 5. Fractal gradients of the flickering, SG and HG, from 30 RLCs. **(a)**: Histogram of the SGs; **(b)**: Histogram of the HGs; **(c)** Juxtaposition of SGs and HGs in B- and V-band with error bars and marked deviated cases. The rectangle covers the area with $SG > 0.5$ and $HG < 0.2$;

The HG is considered to be a robust parameter of the apparent chaos of the non-cyclic time series, i.e. a robust estimator of the fractal dimension (FD) (Mandelbrot & Wallis 1969). The value of our HG is related to the fractal dimension for 1D process as $FD = 2 - HG - 0.3$. Using the HGs in Table 1, we derive the FDs for RS Oph, T CrB and MWC 560 to be 1.48 ± 0.06, 1.52 ± 0.05 and 1.54 ± 0.16, respectively. (The flickering is not a pure non-cyclic process, though.)

For the Nile River the HG is larger, i.e. the chaos is lower, $FD = 1.23$. For comparison, the HG and the FD for the cyclic series of the Wolf number are 0.43 and 1.27, respectively (G20, Fig. 7). For the quasi-cyclic series of the planetarium visits these are 0.21 and 1.49 (G20, Fig. 7), similar to those for RS Oph.

Figure 5 represents the distributions of the SGs and the HGs of the FLCs. The average skewness and kurtosis are collected in Table 1. These values depend somewhat on the goodness of the LLC fits, but they show other specific particularities of the flickering of MWC 560. The SGs are typically larger than 0.5 (Fig. 5a) and the HGs are less than 0.2 (Fig. 5b). The respective rectangle in Fig. 5c contains 18/30=3/5 of the points. In comparison, for RS Oph (G20) and T CrB (G21), the same rectangles contain about 1/5 of the points. The flickering of MWC 560 therefore frequently contains a large contribution of non-sharp shots with short autocorrelation time.

The asymmetry function (AF) is introduced in G20 for any time window Θ by the empirical dimensionless asymmetry parameter:

$$AF_j(\Theta) = < (\delta u_{\max} - \delta u_{\rm med}) \ / \ (\delta u_{\rm med} - \delta u_{\min}) >_j \ . \qquad (4)$$

The AFs are shown in Figs. e by solid curves. Another AF, defined by the skewness A, has a similar but too complex behaviour, especially on the short time scale (G20).

At large windows the AF (Eq. 4) usually decreases slowly from positive to negative values. However, while the window contains 3–6 adjacent FLC points, in 2–7 min time window, the AF is clearly positive (Figs. e). On such time

scales the FLC frequently grows up with an increasing rate or falls down with a decreasing rate (see G20, Fig. 4c and Fig. 10). In the majority of the FLCs, at a little bit larger time window, the AF poses a well defined breakdown time-point (BT). The BTs are marked by verticals in Figs. e. The **BT of the AF** appears as an estimator of the half-period of the shortest QP-like fluctuation. The BT depends on the time resolution of the run and this proves useful (see Fig. 9a).

The autocorrelation function (CF) characterizes the change of the mutual CC of the FLC values upon dependence on the time lag (shift) τ:

$$CF_j(\tau) =< \delta u(t+\tau) \times \delta u(t) >_j \ . \tag{5}$$

By definition $CF = 1$ at $\tau = 0$. When τ is small and increases, the CF decreases. It is characterized by the CF time – the time lag τ at which the CF takes firstly zero value. If the FLC does not have a significant large scale trend, but FLC has QPs, at larger τ, the CF fluctuates. The positions of the maxima of the CF correspond to QPs (Figs. 1f, 2f).

The CF requires equally spaced data. For this reason, only for the CF, every FLC is re-sampled with a step equal to the average resolution time $t_{\rm M}$ of the FLC. The re-sampling of the FLC is not recommended in general, because it ignores the peaks of the FLC, increasing the SG and decreasing the HG.

Figures f show CFs with their CF times, marked by the leftmost verticals. The CF maxima, that confirm the QPs, detected by the SF minima, are marked by verticals as in the SF in Figs. d.

3. Quasi-periods and modes

In this paper the QPs are detected, as in G20 and G21, through the FLCs by coinciding minima of the SF (Eq. 2) and maxima of the CF (Eq. 5). Long SF (or CF) may show local minima (or maxima) corresponding to $2P$, $3P$, etc., but we take into account only the shortest and well pronounced QP. In Figs. d and Figs. f these QPs are marked by solid verticals. If a larger QP corresponds to $2P$, $3P$, etc., it is only marked by a dashed vertical.

The FLCs, flattened by polynomials of 1–3rd degree, are obligatory for detection of the "main" QPs, with lengths 20–100 min. The detectability of the longest QPs depends on the monitoring time $T_{\rm M}$. Here the longest QPs found are shorter than $\approx (2/3)T_{\rm M}$. In G20, Fig. 14a, we had $\approx (3/4)T_{\rm M}$.

We additionally derive flattened FLCs by polynomials of 5–9th degree to evaluate shorter QPs with lengths 10–30 min. Figure 4c shows the distributions of the skewness and the kurtosis of both types of FLCs.

Figure 6 shows the distribution of 51 QPs p. They are found in this work from single LCs, by a main and an additional search. The QPs of the type $2P$, $3P$, etc., if they appear together in a single FLC, are ignored.

MWC 560 shows 8 modes of 60 QPs, at 11.9, 15.3, 22.9, 30.8, 40.1, 51.2, 67.6 and 98 min. Their regularity obeys the power function:

$$P_M = 12.1 \times 1.34^M \quad \text{or} \quad \lg P = 1.08 + 0.093 \times M. \tag{6}$$

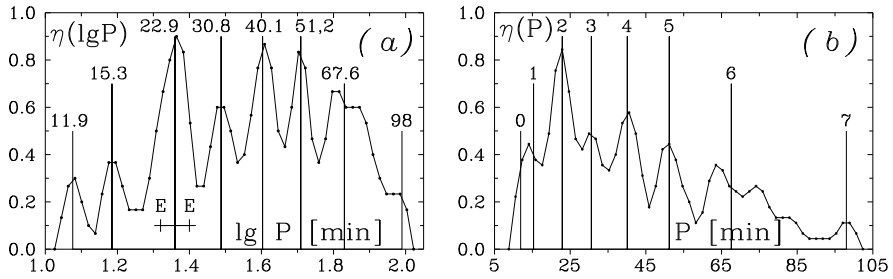

Fig. 6. Joint distributions $\eta(.)$ of 51 QPs p of MWC 560 over a logarithmic time scale **(a)** and over a linear time scale **(b)**. The revealed 8 QP modes are marked by vertical segments. The horizontal segment EE shows the estimated QP error bar.

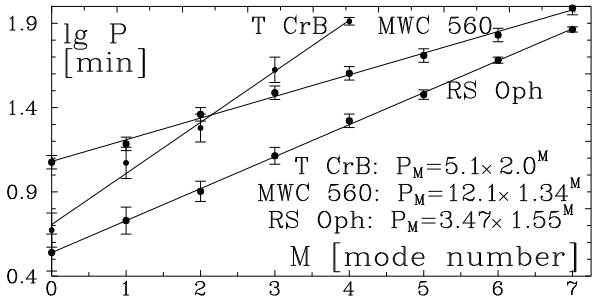

Fig. 7. Regularity of 8 QP modes of RS Oph (G20), 5 QP modes of T CrB (G21) and 8 QP modes of MWC 560 (this work) in respect of (arbitrary) mode numbers M. The respective power functions are implemented.

The mode number $M = 0$ is chosen here to be $P = 12.1$ min. The most populated mode corresponds to QP of 23 min. For T CrB it is 20 min and for RS Oph it is 21 min.

The distributions of the QPs in Fig. 6 are similar to the relevant distributions for RS Oph (G20) and T CrB (G21), but the regularities (near-commensurabilities) in these 3 systems of modes are too different.

Figure 7 juxtaposes the regularities of the QP modes of the regarded 3 symbiotic stars. The logarithms of the QP modes of RS Oph, T CrB and MWC 560 follow "resonances", approximately 3:2, 2:1 and 4:3, respectively.

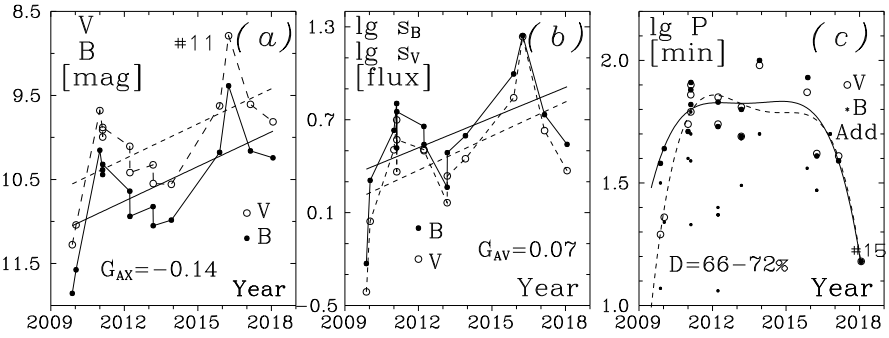

Fig. 8. Behaviour of MWC 560 in B- and V-band over the years. **(a)**: Changes of the average magnitude of the run; **(b)**: Changes of the flux SD and the RD of the LLC; **(c)**: Changes of the main QPs, 15 in B- and 15 in V-band, fitted by polynomials of 4th degree. The small dots, noted as "Add", show the additionally found 21 shorter QPs, not used for the fits. D is the determination coefficient of the polynomials.

4. Other results

This section represents the behaviour of the flickering over the years, the estimation of the minimal QP, as well as the use of the flux SD (from the LLC) as an indicator of the magnitude and the radius of the flickering source.

Figure 8 illustrates the variations of 3 parameters of MWC 560 in the period 2009–2018. Figure 8a shows the step-like changes of the magnitudes with an average gradient of -0.14 mag/yr. The point #11 corresponds to the eruption in 2016. Figure 8b shows that the logarithms of the flux SDs, s_B and s_V, change synchronously with the magnitudes, with an average gradient of 0.07 yr^{-1}. Figure 8c shows the trend of the length of the main QP with a plateau in 2011-2017. The main QPs are shorter around the beginning (2010) and around the end (2018) of the observations.

Figure 9a shows the correlation between the average time resolution of the run t_M and the BT of the AF. The intercept of the fit at $t_M = 0$, $P_0/2$, estimates the typical half-period of the shortest twinkle. For our cataclysmic stars the values of P_0 coincide approximately with the prolongation of the mode system (Fig. 7) towards the shorter periods. For RS Oph (G20, Fig .11b) $P_0 = 2.6$ min is close to $P = 2.28$ for $M = -1$. For T CrB (G21, Fig 9a) $P_0 = 1.2$ min is close to $P = 1.76$ for $M = -2$. For MWC 560 (this work, Fig. 9a) $P_0 = 3.46$ min is close to $P = 3.75$ for $M = -4$.

The narrow correlations between the logarithm of the SD flux and the logarithm of the average flux for 9 interacting stars is found in Z16. The question about the accuracy of the flux SD as an indicator of the magnitude or the size of the flickering source arises. The answer is shown in Figs. 9c and 9d. The use of RD flux (not shown) gives the same results. Data for the magnitude and the size of the flickering source are given kindly by Z21.

Figure 9b shows that in the case of MWC 560 the flux SDs of the LLCs, $\lg s_B$ and $\lg s_V$, indicate the B- and V-magnitudes of the flickering source within a low accuracy, 0.33–0.34 mag.

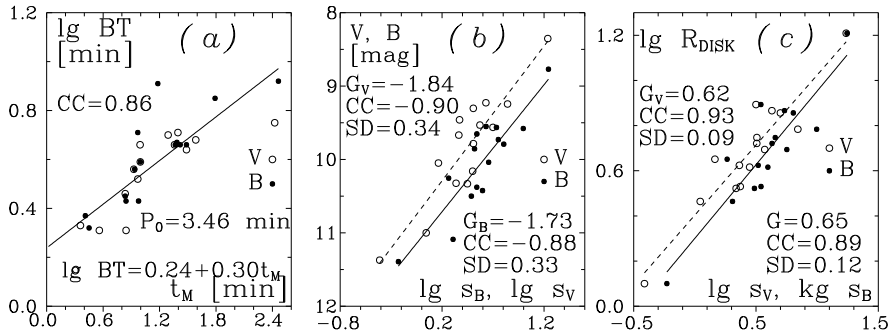

Fig. 9. (a): Correlation between the average time resolution of the run t_M and the BT of the AF (Eq. 4, Figs. e); **(b)**: Correlation between the logarithms of the SDs of the LLCs and the magnitude of the flickering source; **(c)**: Correlation between the flux SDs of the LLCs and the radius of the flickering source (in solar radii) in log-log coordinates.

Figure 9c shows, similarly to Fig.9b, that $\lg s_B$ and $\lg s_V$ indicate the radius of the flickering source with a logarithmic accuracy of about 0.1, i.e. with a low linear accuracy of about 26%

Conclusions

We used 30 runs of MWC 560, 15 B- and 15 V-band, in 2009–2018. We applied a system of statistical and fractal tools to analyse the flickering. The details of the method are illustrated in the on-line Appendix for every run. The conclusions are as follows:

1. We find that the flickering of MWC 560 is similar by flux standard deviations to 9 analogous stars (including RS Oph and T CrB), studied in Z16. However, the relevant flux range deviations ("the halves of the peak-to-peak amplitudes") are lower by 10–20%, i.e. short and sharp deviations are almost absent (Figs. 3, 4a, 4b).

2. The logarithms of the flux standard deviations and the flux range deviations pose correlation coefficients of 0.99 (Figs. 3c, 3d). These parameters also indicate the magnitude and the size of the flickering source of MWC 560 with a low accuracy of 0.34 mag and 26%, respectively (Figs. 9b, 9c).

3. The kurtosis obeys a quadratic correlation with the skewness (Fig. 4c). In comparison with RS Oph and T CrB the flickering of MWC 560 shows an intermediate mean skewness, i.e. some excess of short positive deviations, and a lower mean kurtosis, i.e. again an evidence of some deficit of large deviations.

4. The structure gradients of the flickering of RS Oph, T CrB and MWC 560 are 0.48, 0.34 and 0.61, respectively, i.e. the flickering of MWC 560 contains

the most significant contribution of non-sharp shots (Fig. 5). The fractal dimensions of the flickering, simultaneously derived by the Hurst gradients, are 1.48, 1.52 and 1.54, respectively, i.e. the flickering of MWC 560 poses a little bit higher chaos.

5. We reveal quasi-periods in the flickering of RS Oph, T CrB and MWC 560 by minima of the structure functions and by relevant maxima of the autocorrelation functions. The most populated modes of the QPs correspond to 21 min, 20 min and 23 min, respectively. The distribution of the revealed 51 QPs of MWC 560 shows 8 modes (Fig. 6) which accurately obey a power function with a base of $\approx 4/3$. For RS Oph and T CrB the bases are $\approx 3/2$ and ≈ 2, respectively (Fig. 7). For unknown reasons the regularities of the flickering modes of these 3 stars are very different.

6. Our empirical asymmetry function (Eq. 4) shows evidence that positive twinkles dominate at short time scale (3–6 min) in the flickering of RS Oph, T CrB and MWC 560. The contribution of these twinkles decreases sharply at a breakdown time point at a little bit longer time scale. The logarithms of these time points correlate with the resolution time of the run (Fig. 9a) and the intercept of the relevant linear fit is an estimator of the half of the shortest observable QPs, $P_0/2$. For the regarded stars the values of P_0 are 2.6 min, 1.2 min and 3.5 min, respectively. These QPs fall approximately on the prolongations of the QP mode regularities towards the short times.

Acknowledgments: This work is supported by the grant КП-06-Н28/2 08.12.2018 of the Bulgarian National Science Fund.

References

Bachev, R., Boeva, S., Georgiev, T. et al. 2011, *Bulg. Astron. J.*, 16, 31
Bond, H. E., Pier, J., Pilachowski, C., et al. 1984, *BAAS16, 516*
di Clemente, A., Giallongo, E., Natali, G. et al. 1996, *ApJ*, 463, 466
Falconer K. 1997, *Techniques in Fractal Geometry*, John Willey & Sons
Gantchev, G., Valcheva, A., Nedialkov, P., Ovcharov, E. 2017, *Bulg. Astron. J.*, 26, 16
Georgiev, T. 2022, *Bulg. Astron. J.*, 36, in print.
Georgiev, T., Zamanov, R., Boeva, S. et al. 2020, *Bulg. Astron. J.*, 33, 3 [G20]
Georgiev, T., Boeva, S., Latev, G. et al. 2021, *Bulg. Astron. J.*, 34, 10 [G21]
Goranskij, V. P., Zaharova, A. V., Barsukova, E. A., et al. 2018, *Astron. Telegram 12227, 1*
Gromadzki, M., Mikołajewska, J., Whitelock, P. A., et al. 2007, *A&A, 463, 703*
Hurst, H.E. 1951, *Transactions of American Society of Civil Engineers*. 116: 77
Kawaguchi, T., Mineshige, S., Umemura, M., Turner, E. L. 1998, *ApJ* 504, 671
Lafler, J., & Kinman, T.D. 1965, *ApJS* 11, 216
Lucy, A. B., Knigge, C., & Sokoloski, J. L. 2018, *MNRAS, 478, 568*
Lucy, A. B., Sokoloski, J. L., Munari, U., et al. 2016a, *Astron. Telegram 8832, 1*
Lucy, A. B., Sokoloski, J. L., Munari, U., et al. 2020, *MNRAS, 492, 3107*
Lucy, A. B., Weston, J. H. S., & Sokoloski, J. L. 2016b, *Astron. Telegram 8957, 1*
Mandelbrot B. B. 1982, *The fractal Geometry of Nature*, Freeman, New York
Mandelbrot, B. B., Wallis, J. R. 1968, *Water Resources Research*, 4, 909991
Mandelbrot, B. B., Wallis, J.R. 1969, *Water Resources Research*, 5, 967988
Munari, U., Dallaporta, S., Castellani, F., et al. 2016a, *New A, 49, 43*
Munari, U., Righetti, G., Dallaporta, S., et al. 2016b, *Astron. Telegram 8653, 1*
Russ J.C. 1994, *Fractal Surfaces*, Plenum Press, New York & London
Schmid, H. M., Kaufer, A., Camenzind, M., et al. 2001, *A&A, 377, 206*
Tomov, T., Kolev, D., Georgiev, L., et al. 1990, *Nature, 346, 637*
Tomov, T., Kolev, D., Ivanov, M. et al. 1996, *A&AS*, 116, 1
Zamanov, R. K., Boeva, S., Latev, G., et al. 2016, *MNRAS, 457, L10* [Z16]
Zamanov, R. K., Boeva, S., Stoyanov, K. A., et al. 2021, *Astron. Nachr., 342, 531* [Z21]
Zamanov, R., Gomboc, A., & Latev, G. 2011, *Bulg. Astron. J., 16, 18*
Zamanov, R. K., Gomboc, A., Stoyanov, K. A., et al. 2010, *Astron. Nachr,, 331, 282*
Zamanov, R., & Marziani, P. 2002, *ApJ, 571, L77*